Evaluation of Finite-Rate Surface Chemistry Models for Simulation of the Stardust Reentry Capsule

Hicham Alkandry[*], Erin D. Farbar[†], and Iain D. Boyd[‡]

Department of Aerospace Engineering, University of Michigan, Ann Arbor, Michigan, USA

Gas-surface interactions can have a significant effect on the aerothermodynamic properties of planetary entry vehicles. Therefore, it is important to evaluate these effects in the numerical analysis of entry flows. The first part of this paper describes the implementation of an existing finite-rate surface chemistry module into a Navier-Stokes solver. The module can simulate the chemical interaction of the hypersonic gas flow with the surface of a planetary entry vehicle, and allows the specification of several different surface reaction types, such as adsorption, Eley-Rideal recombination, Langmuir-Hinshelwood recombination, and sublimation. In the second part of the paper, the effects of using two different surface chemistry models developed by Driver et al. and Park on the numerical predictions of the flow field and surface properties of the Stardust return capsule at the 81 km trajectory point are evaluated. Both models include carbon oxidation, and one of the main differences between the two is that a mechanism for carbon nitridation is included in Park's model. The production of CN in Park's model causes the mass blowing rate due to the removal of bulk carbon to be greater by as much as 45% compared to Driver's model. The heat transfer to the surface for Park's model is approximately 20% less than for Driver's model. When the carbon nitridation reaction is excluded from Park's model, the results show better agreement in the heat flux and blowing rate as compared to Driver's model.

Nomenclature

Av	Avogadro's number, particles/mol
D_k	Diffusion coefficient of species k, m^2/s
E_{ad}	Energy barrier for adsorption, J/mol
E_{ER}	Energy barrier for Eley-Rideal recombination, J/mol
E_{LH}	Energy barrier for Langmuir-Hinshelwood recombination, J/mol
E_{sub}	Energy barrier for sublimation, J/mol
k_b	Backward reaction rate, units vary
k_f	Forward reaction rate, units vary
K_a	Activity-based equilibrium constant
K_c	Concentration-based equilibrium constant, units vary
$\dot{m}$	Mass blowing rate due to surface reactions, kg/m^2/s
M_k	Molar weight of species k, kg/mol
N_g	Number of gas phase species
N_{nb}	Number of bulk species
N_R	Number of surface reactions
p_n	Pressure at first cell face away from wall, Pa
p_w	Pressure at the wall, Pa
Ru	Universal gas constant, J/mol/K
T_a	Activation temperature for chemical reactions, K
T_c	Controlling temperature for chemical reactions, K

---

[*]Research Associate, Member AIAA. Email: halkandr@umich.edu
[†]Research Associate, Member AIAA.
[‡]James E. Knott Professor of Engineering, Fellow AIAA.

American Institute of Aeronautics and Astronautics

T_{tr}	Translational/rotational temperature, K
T_{ve}	Vibrational/electronic/electron temperature, K
$\bar{v}_k$	Thermal speed of gas phase species k, m/s
$\bar{v}_{2D,k}$	Two-dimensional thermal speed of mobile species k, m/s
v_n	Velocity at first cell face away from wall, m/s
v_w	Wall normal velocity, m/s
$\dot{w}_k$	Molar production rate of species k, mol/m^2/s
Y_k	Mass fraction of species k
γ_k	Gas phase reactant loss efficiency
ρ_n	Gas phase density at first cell face away from wall, kg/m^3
ρ_w	Gas phase density at the wall, kg/m^3
ϕ_k	Surface site density of phase k, mol/m^2

I. Introduction

Planetary entry vehicles are required to sustain very high aerodynamic heat fluxes when entering an atmosphere. For this reason, many vehicles currently being designed employ a thermal protection system (TPS). Accurate simulation of the aerothermal environment expected during atmospheric entry for these vehicles requires models for complicated physical processes, such as nonequilibrium surface chemistry. This in turn requires a coupling between the flow field solver and the surface mass, momentum, and energy boundary conditions. Inputs for the surface boundary conditions can be obtained from analytical models, or detailed material response models. The primary purpose of this work is to develop a coupling interface between an existing Finite-Rate Surface Chemistry (FRSC) Module developed by Marschall and MacLean[1, 2] and the LeMANS CFD code developed at the University of Michigan.[3, 4] This will enable tightly-coupled CFD solutions to be generated that include the effects of nonequilibrium surface chemistry.

The second goal of this study is to evaluate the effects of nonequilibrium surface chemistry models by using LeMANS with the FRSC Module to simulate the flow around the Stardust entry capsule. The Stardust payload was launched in 1999 on a mission to collect samples from interstellar dust and the tail of the Comet Wild-2, and return them to Earth. The Stardust sample return capsule, shown schematically in Figure 1(a), landed in the Utah desert in January of 2006, and its Earth entry trajectory[5] is presented in Figure 1(b). The Stardust spacecraft then continued its travel through the solar system, on a mission to image Comet Tempel-1. It was decommissioned after completing that final mission in March 2011. The Stardust mission represents the first ever return of a sample from a comet; a significant milestone in the human exploration of space. With an entry velocity of 12.6 km/s, the capsule was also the fastest man-made object ever to enter the Earth's atmosphere, providing a unique test case to evaluate numerical simulations. In order to protect the vehicle from the extreme entry conditions, the TPS for the Stardust capsule employed a phenolic-impregnated carbon ablator (PICA),[6] which is a lightweight material with a density of approximately 240 kg/m^3.

The paper is presented in two sections. The first part of the paper describes the formulation of the FRSC Module and the coupling to LeMANS. This section also presents a comparison between the solutions obtained using LeMANS and the NASA DPLR code[7] for two different test cases in order to verify the coupling between LeMANS and the FRSC Module. The second part of the paper presents flow field predictions for the Stardust entry capsule at the 81 km trajectory point obtained using two different surface chemistry models developed by Driver et al.[8, 9] and Park.[10, 11, 12] In this section, details regarding the numerical setup for the simulations are provided first. Then, comparisons of the predicted Stardust flow field and surface properties using the two surface chemistry models are described. Finally, the paper presents some conclusions drawn from these comparisons and possible future work directions.

II. Finite-Rate Surface Chemistry Formulation

The FRSC Module developed by Marschall and MacLean[1, 2] models the chemical interaction of the hypersonic gas flow with the surface of a planetary entry vehicle. The FRSC Module allows for the definition of three distinct environments: gas, surface, and bulk. The surface and bulk environments can have any number of phases, which represent physically and chemically distinct regions. The gas environment can only have a single phase. Surface reactions may only occur at active sites that can either be empty or filled with

American Institute of Aeronautics and Astronautics
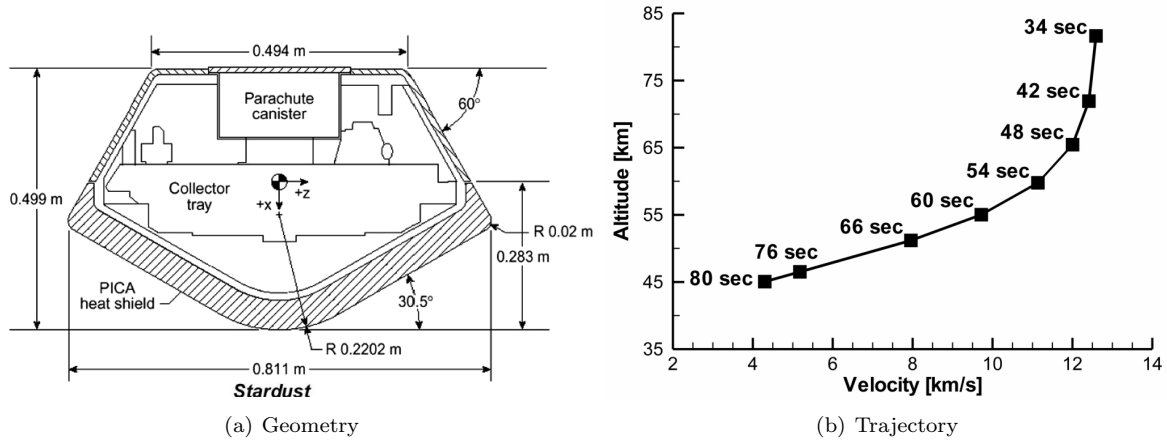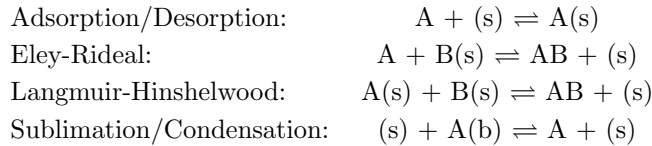
(a) Geometry (b) Trajectory

Figure 1: Stardust return capsule geometry and entry trajectory.

an adsorbed species on a specific surface phase. The total number of reaction sites is conserved and sites may neither be created nor destroyed. The number of reaction sites (i.e. site density) is a property of the surface and is defined as a user input. The FRSC Module allows the specification of several different reaction types. These include,

Adsorption/Desorption:	A + (s) $\rightleftharpoons$ A(s)
Eley-Rideal:	A + B(s) $\rightleftharpoons$ AB + (s)
Langmuir-Hinshelwood:	A(s) + B(s) $\rightleftharpoons$ AB + (s)
Sublimation/Condensation:	(s) + A(b) $\rightleftharpoons$ A + (s)

In the previous examples, (s) represents an empty active site, A(s) is an adsorbed particle, and A(b) is a bulk species. The FRSC Module also allows for the specification of several other reaction processes that do not strictly fit into the categories given above (e.g. oxidation and nitridation).

The general form for reaction i can be expressed as,

$$\sum_{k=1}^{K} \nu'_{ki} A_k \rightleftharpoons \sum_{k=1}^{K} \nu''_{ki} A_k \tag{1}$$

where ν'_{ki} and ν''_{ki} are the stoichiometric coefficients for species k on the reactant and product sides, respectively. The net production rate for species k from all surface reactions is,

$$\dot{w}_k = \sum_{i}^{N_R} \dot{w}_{ki} \tag{2}$$

where the reaction-specific production rate, $\dot{w}_{ki}$, is given by,

$$\dot{w}_{ki} = (\nu''_{ki} - \nu'_{ki}) \left(k_{fi} \prod_{k=1}^{K} X_k^{\nu'_{ki}} - k_{bi} \prod_{k=1}^{K} X_k^{\nu''_{ki}} \right) \tag{3}$$

where k_{f_i} and k_{b_i} are the forward and backward rates for reaction i, respectively, and X_k is the concentration of species k at the surface.

The forward reaction rates for surface processes are specified using kinetics-based formulations for specific reaction types as,
Adsorption:

$$k_f = \left[\frac{\bar{v}_A}{4\phi_s^{\nu_s}} \right] S_0 \exp\left(-\frac{E_{ad}}{RuT} \right) \tag{4}$$

American Institute of Aeronautics and Astronautics

Eley-Rideal:

$$k_f = \left[\frac{\bar{v}_A}{4\phi_s^{\nu_s}} \right] \gamma_0 \exp\left(-\frac{E_{ER}}{RuT} \right) \tag{5}$$

Langmuir-Hinshelwood:

$$k_f = \left[\bar{v}_{2D,A} \sqrt{Av} \right] \phi_s^{1.5-\nu_s} C_{LH} \exp\left(-\frac{E_{LH}}{RuT} \right) \tag{6}$$

Sublimation:

$$k_f = \left[\frac{\bar{v}_A}{4\phi_s^{\nu_s} RuT} \right] \gamma_{sub} \exp\left(-\frac{E_{sub}}{RuT} \right) \tag{7}$$

The thermal velocities used in the rate expressions are given by,

$$\bar{v}_A = \sqrt{\frac{8RuT}{\pi M_A}} \tag{8}$$

and

$$\bar{v}_{2D,A} = \sqrt{\frac{\pi RuT}{2M_A}} \tag{9}$$

The temperature used in these expressions is the translational temperature of the gas at the surface, which is equal to the wall temperature for this work. This approach of defining the forward reaction rates is more insightful than using Arrhenius-type expressions since the Arrhenius reaction parameters may be difficult to relate to physical, chemical, or kinetic processes. Note, however, that the FRSC Module also allows for Arrhenius-type formulations for the forward rates.

The backward rate for reaction i is determined based on the forward rates and the concentration-based equilibrium constant by,

$$k_{b,i} = \frac{k_{f,i}}{K_{c,i}} \tag{10}$$

The concentration-based equilibrium constant is related to the activity-based equilibrium constant by,

$$K_{c,i} = K_{a,i} \left(\frac{P_{ref}}{RuT} \right)^{\nu_{g,i}} \tag{11}$$

where P_{ref} is a reference pressure of 10^5 Pa, which is the same value used in the NASA Glenn thermodynamic database,[13] and $\nu_{g,i}$ is the net stoichiometric exponent for gas species equal to $\sum (\nu_{ki}'' - \nu_{ki}')$. The activity-based equilibrium constant is related to changes in the Gibbs energy of formation and can be calculated directly if the necessary thermodynamic properties are available by,

$$K_{a,i} = \exp\left[-\frac{\Delta G_i^0(T)}{RuT} \right] \tag{12}$$

where the change in Gibbs energy of formation, $\Delta G_i^0(T)$, can be obtained from databases, such as the NASA Glenn thermodynamic database.[13] However, the difference between the Gibbs energy of formation of an occupied active site and an empty active site may not be available for most species. For these cases, either the backward rate $k_{b,i}$ or the concentration-based equilibrium constant $K_{c,i}$ must be specified in addition to the forward rate for each adsorption reaction based on statistical thermodynamics and/or kinetic theory. Then, the missing thermodynamic data for occupied and empty active sites can be calculated using Equations 11 and 12. The calculated change in Gibbs energy of formation can then be used with the available thermodynamic data for gas and solid phase species to calculate the constants for all other surface reactions. Additional details regarding the FRSC Module are provided in Ref. 1.

III. Coupling to a Navier-Stokes Solver

A. Navier-Stokes Solver

The numerical simulations are performed using the CFD code LeMANS, which is developed at the University of Michigan.[3,4] This three-dimensional, parallel code solves the laminar Navier-Stokes equations on

American Institute of Aeronautics and Astronautics

unstructured computational grids including thermo-chemical nonequilibrium effects. In LeMANS, the flow is modeled assuming that the continuum approximation is valid. For this study, it is also assumed that the translational and rotational energy modes can be described by a single temperature, T_{tr}, and that the vibrational, electronic, and electron translational energy modes are described by a different temperature T_{ve}. The mixture transport properties are calculated using one of two models. The first uses Wilke's semi-empirical mixing rule[14] with species viscosities calculated using Blottner's curve fits[15] and species thermal conductivities determined using Eucken's relation.[16] The other model uses Gupta's mixing rule with species viscosities and thermal conductivities calculated using collision cross section data.[17] In this study, the mass diffusion fluxes of heavy particles are modeled using Fick's law, and the diffusion flux of electrons is calculated assuming ambipolar diffusion.[18] The mass diffusion coefficient for each species is replaced by a single binary coefficient calculated by assuming a constant Lewis number.

In LeMANS, the set of governing equations are solved using the finite-volume method applied to unstructured grids with second order spacial accuracy. LeMANS can simulate two-dimensional and axisymmetric flows using any mixture of quadrilateral and triangular mesh cells, and three-dimensional flows using any mixture of hexahedra, tetrahedra, prisms, and pyramids. A modified Steger-Warming Flux Vector Splitting scheme[19] is used to discretize the inviscid fluxes across cell faces, which is less dissipative and produces better results in boundary layers compared to the original scheme. The viscous terms are computed using cell-centered and nodal values. The viscous stresses are modeled assuming a Newtonian fluid and Stokes' hypothesis, and the heat fluxes are modeled according to Fourier's law for all temperatures. LeMANS is parallelized using METIS[20] to partition the computational mesh, and the Message Passing Interface (MPI) to communicate the necessary information between processors.

B.   Implementation of the FRSC Module

Given the pressure, temperature, and species concentrations at the surface obtained from LeMANS, the FRSC Module computes the species production rates, the blowing rate due to the removal of bulk species by surface reactions, and the steady-state surface coverage (i.e. distribution of adsorbed species). These values are then communicated to LeMANS. In order to model a reacting surface in a CFD code, the equations of conservation of mass, momentum, and energy must be satisfied at the surface. The species mass conservation equations,

$$-\rho_w D_k \frac{\partial Y_k}{\partial n}\Big|_w + \rho_w v_w Y_{k,w} = M_k \dot{w}_k \tag{13}$$

momentum conservation equation,

$$p_n + \rho_n v_n^2 = p_w + \rho_w v_w^2 \tag{14}$$

and energy conservation equation,

$$\kappa_{tr}\nabla T_{tr}|_w + \kappa_{ve}\nabla T_{ve}|_w + \sum_{k=1}^{N_g} \rho D_k h_k \nabla Y_k|_w = \dot{m}_b(h_w - h_a) + \sigma\epsilon T_w^4 \tag{15}$$

are solved using the species production rates ($\dot{w}_k$) and mass flux of bulk species ($\dot{m}_b$) computed using the FRSC Module. These relations are derived assuming steady-state ablation in which the ablating surface, char front, pyrolysis front, and unaffected front all recede at the same rate.[21] The enthalpy of the virgin material in Equation 15, h_a, is a user-defined input. The set of conservation equations is solved iteratively using a Newton-type method to obtain the species mass fractions ($Y_{k,w}$), gas density (ρ_w), gas normal velocity (v_w), and gas temperature (T_w) at the wall. For this study, the vibrational temperature at the wall is assumed to be equal to the translational temperature. The loss efficiency for a gas phase reactant k (i.e. the fraction of collisions with the surface that result in its removal from the gas environment) can be calculated by,

$$\gamma_k = \frac{4\dot{w}_k}{X_k \bar{v}_k} \tag{16}$$

The concentrations of the surface species are updated at each solver iteration using Equation 17,

$$\frac{\partial X_s}{\partial t} = \dot{w}_s \tag{17}$$

American Institute of Aeronautics and Astronautics

where the time step is equal to the global time step of the simulation.

The FRSC Module includes a rudimentary form of blowing to simulate pyrolysis gases emitted from the surface. This approach, however, has not been included in the current implementation. As a result, the only contribution to the mass blowing rate at the surface is due to the removal of species from the bulk environment caused by surface reactions (e.g. oxidation, nitridation, and sublimation). This blowing rate is a function of the production rates of bulk species and is calculated by,

$$\dot{m}_b = \rho_w v_w = -\sum_{k=1}^{N_{nb}} M_k \dot{w}_k \tag{18}$$

Although the FRSC Module is designed to be used in a coupled, fully-implicit manner to the CFD code, an explicit coupling scheme is currently used in this work. This means that the values of the species mass fractions from the previous iteration of the solver are used to calculate $\dot{w}_k$ and $\dot{m}_b$ in order to set the boundary conditions at the current iteration. This is the same approach adopted in Ref. 22 and works relatively well for steady-state problems.

C. Test Cases

1. Air/Silica System

Two test cases have been chosen to verify the coupling of the FRSC Module to LeMANS. The first case considers the flow of reacting air over a 2.0 m diameter cylinder with a catalytic silica surface. This case was originally studied by Sorensen et al.[22] to investigate the sensitivity of the heat transfer along the surface of a reentry vehicle to the rates of the surface reactions, and was also used by MacLean et al.[2] to test the implementation of the FRSC Module in the DPLR code. The freestream conditions for this case are: $\rho = 0.001$ kg/m^3, $U = 6000$ km/s, and $T_{tr} = T_{ve} = 200$ K. The surface temperature is assumed to be constant and equal to 2250 K. The mixture transport properties are calculated using Wilke's mixing rule with Blottner's curve fits for species viscosities and Eucken's relation for species thermal conductivities. The Lewis number is constant and equal to 1.4. Table 1 presents the surface chemistry model used for this test case. The model includes nine reactions, and accounts for the adsorption of atomic oxygen and nitrogen onto the surface and subsequent recombination via both Eley-Rideal and Langmuir-Hinshelwood mechanisms. The initial density of available empty surface sites is assumed to be equal to 7.5×10^{-6} mol/m^2. Qualitative flow field temperature contours calculated using LeMANS are shown in Figure 2.

Table 1: Surface chemistry model for the air/silica test case.

#	Reaction	Type	Parameter	E [kJ/mol]
1	O + (s) $\rightleftharpoons$ O(s)	ad	$S_0 = 0.05$	0
2	N + (s) $\rightleftharpoons$ N(s)	ad	$S_0 = 0.05$	0
3	O + O(s) $\rightleftharpoons$ O$_2$ + (s)	ER	$\gamma_0 = 0.001$	9
4	N + N(s) $\rightleftharpoons$ N$_2$ + (s)	ER	$\gamma_0 = 0.001$	9
5	O + N(s) $\rightleftharpoons$ NO + (s)	ER	$\gamma_0 = 0.001$	9
6	N + O(s) $\rightleftharpoons$ NO + (s)	ER	$\gamma_0 = 0.001$	9
7	2O(s) $\rightleftharpoons$ O$_2$ + 2(s)	LH	$C_{lh} = 0.1$	300
8	2N(s) $\rightleftharpoons$ N$_2$ + 2(s)	LH	$C_{lh} = 0.1$	300
9	O(s) + N(s) $\rightleftharpoons$ NO + 2(s)	LH	$C_{lh} = 0.2$	300

Figure 3(a) shows comparisons of surface heat transfer calculated by LeMANS to the results obtained by MacLean et al. using DPLR.[2] The figure also shows heat transfer comparisons for two other cases performed by assuming a non-catalytic wall (no surface recombination) and a super-catalytic wall (recombination to freestream composition) boundary conditions. The agreement between the heat transfer predictions by LeMANS and DPLR for all cases is excellent. The results show that the heat flux for the finite-rate model is between the solutions for the non-catalytic and super-catalytic wall conditions, and the surface becomes

American Institute of Aeronautics and Astronautics

more catalytic near the shoulder than at the stagnation point. Figure 3(b) shows a comparison of the steady-state concentration of the adsorbed species along the cylinder surface predicted by LeMANS and DPLR. The steady-state surface coverage is mainly dominated by atomic oxygen at these conditions. Once again, the agreement between LeMANS and DPLR is excellent.
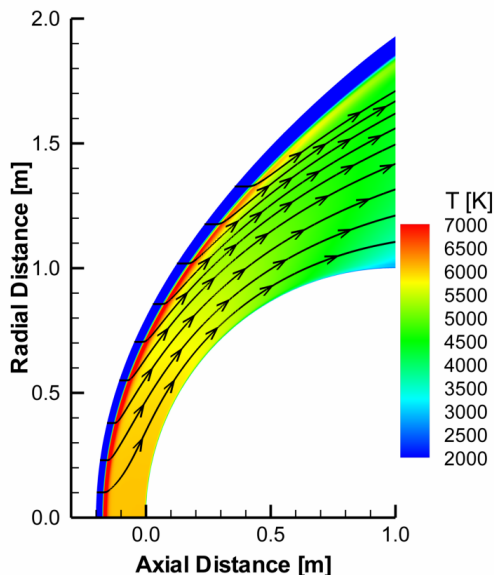

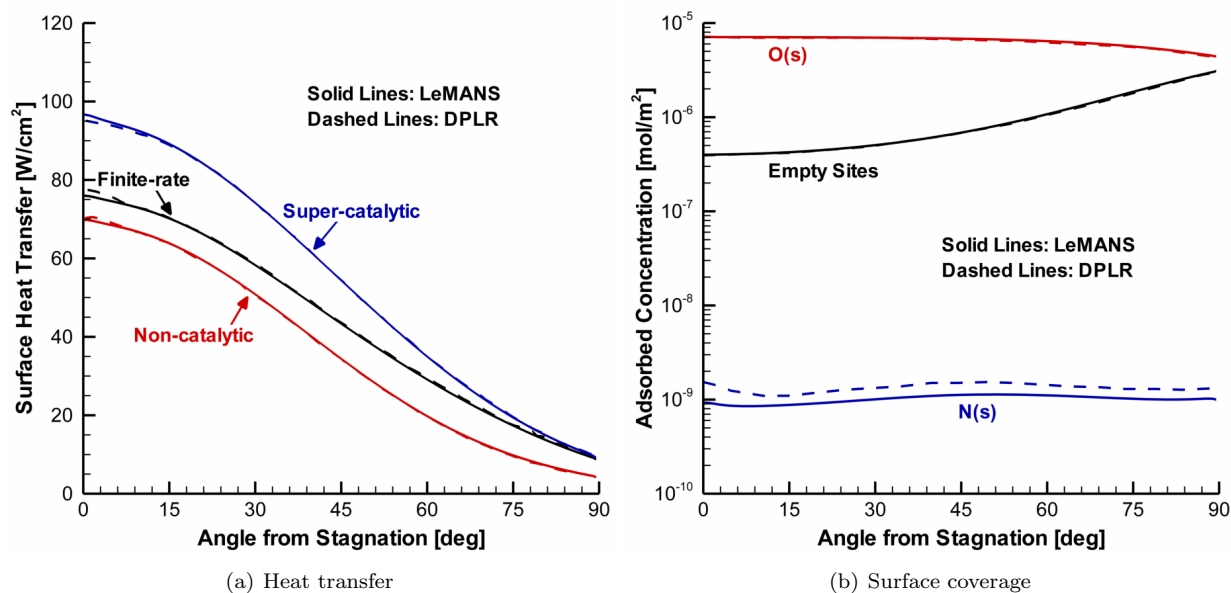Figure 2: Temperature contours for the air/silica test case.

(a) Heat transfer

(b) Surface coverage

Figure 3: Comparison of surface heat transfer and steady-state surface coverage between LeMANS and DPLR for the air/silica test case.

2. Air/Carbon System

The second case used to test the implementation of the FRSC Module in LeMANS considers the flow of reacting air over a 4-inch diameter iso-Q geometry composed of FiberForm, which is the carbon preform used in the fabrication of PICA. The iso-Q geometry is designed to experience relatively constant heat flux

American Institute of Aeronautics and Astronautics

and recession rate along the surface. The freestream conditions are: $\rho = 0.00345$ kg/m^3, $U = 3860$ m/s, $T_{tr} = 1470$ K, and $T_{ve} = 1787$ K. The freestream species mass fractions are: $Y_{N_2} = 0.710$, $Y_{O_2} = 0.024$, $Y_{NO} = 0.020$, $Y_N = 0.0$, $Y_O = 0.182$, $Y_{CO} = 0.0$, $Y_{Ar} = 0.064$. The surface temperature is calculated assuming radiative equilibrium at the wall with an emissivity of 0.9. The mixture transport properties are calculated using Gupta's mixing rule. The Lewis number is assumed to be equal to 1.4.

Table 2 presents the surface chemistry model used for this test case. In this model, developed by Driver et al.,[8, 9, 2] the oxidation of bulk carbon by atomic oxygen occurs with a constant reaction probability of $\gamma_{ox,O} = 0.90$, and the oxidation of bulk carbon by molecular oxygen occurs with a constant probability of $\gamma_{ox,O_2} = 0.01$. This reaction is mediated by one set of surface sites of type "(s$_1$)", and there is only one bulk carbon phase, denoted "C(b)". This is accomplished in the FRSC Module framework by specifying two irreversible Eley-Rideal type reactions with zero activation energy and $\gamma_0 = 0.90$ and 0.01, respectively. The model also includes the recombination of atomic nitrogen at the surface. The catalysis of nitrogen atoms occurs with a constant recombination probability of $\gamma_{cat,N} = 0.05$. This reaction is modeled as irreversible adsorption and Eley-Rideal reactions with zero activation energy, constant reaction efficiency of $\gamma_0 = 0.05$, and constant sticking coefficient of $S_0 = 0.05$ on a second set of surface sites denoted "(s$_2$)". Two different sets of surface sites are used in this model in order to keep the reaction efficiencies of the two processes (i.e. carbon oxidation and nitrogen catalysis) independent. If only one set is used, the adsorbed nitrogen can occupy a portion of the available empty sites, which reduces the efficiency of the oxidation process. Figure 4 presents flow field temperature contours obtained using LeMANS for this test case.

Table 2: Driver's surface chemistry model.

#	Reaction	Type	Parameter	E [kJ/mol]
1	O + (s$_1$) + C(b) → CO + (s$_1$)	ER	$\gamma_0 = 0.90$	0
2	O$_2$ + 2(s$_1$) + 2C(b) → 2CO + 2(s$_1$)	ER	$\gamma_0 = 0.01$	0
3	N + (s$_2$) → N(s$_2$)	ad	$S_0 = 0.05$	0
4	N + N(s$_2$) → N$_2$ + (s$_2$)	ER	$\gamma_0 = 0.05$	0

Figure 5 presents comparisons of the iso-Q surface properties between LeMANS and DPLR. As expected, the heat transfer is approximately constant along the surface due to the iso-Q geometry. Figure 5(a) shows that the heat flux is equal to approximately 280 W/cm^2, and the temperature is about 2750 K along the surface. The figure shows very good agreement between LeMANS and DPLR, with a maximum difference of less than 3% in the surface heat transfer between the two codes. This agreement can also be observed in the mass blowing rate due to the removal of bulk carbon and the mass fraction of atomic nitrogen along the iso-Q surface shown in Figure 5(b). The difference in the blowing rates predicted by the two codes is also less than 3%. The agreement observed between the solutions predicted by the two codes for these two test cases indicates that the FRSC Module has been properly implemented in LeMANS.

IV.   Stardust Entry Capsule

A.   Numerical Setup

The second goal of this study is to evaluate the effects of two different surface chemistry models using the FRSC Module on the flow field predictions for the Stardust entry capsule. The first model considered in this study was developed by Driver et al.[8, 9] to investigate high recession rates of carbon ablators in arc jet shear tests. The surface reactions are given in Table 2. Driver et al. employed this model to successfully predict the interaction of oxygen on a FiberForm surface. Driver's model does not include carbon nitridation because the arc jet shear tests have indicated that mass removal by nitridation is negligible compared to mass removal by the carbon oxidation reactions.[9] The second model considered in this study is Park's model.[10, 11, 12] The reactions for Park's model are listed in Table 3. The reaction parameters for this model were obtained from Ref. 2. In this model, the oxidation of bulk carbon by atomic oxygen occurs with a reaction probability of $\gamma_{ox,O} = 0.63$ and an activation energy of 9.644 kJ/mol, and the oxidation of bulk carbon by molecular oxygen occurs with a constant probability of $\gamma_{ox,O_2} = 0.50$. The model also includes carbon sublimation, as well as the nitridation of bulk carbon by atomic nitrogen at a constant reaction probability of $\gamma_{ni,N} = 0.30$.
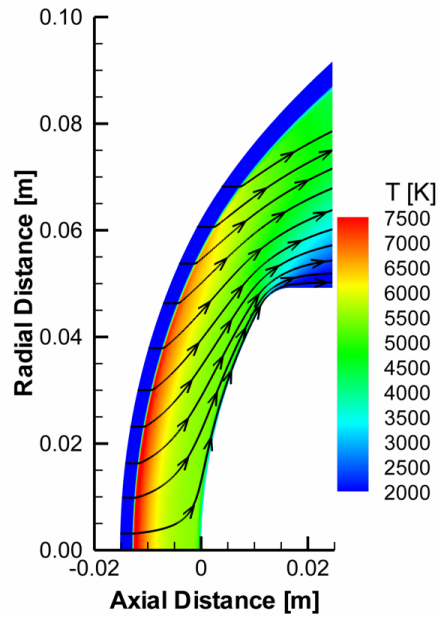
Figure 4: Temperature contours for the air/carbon test case.

(a) Heat transfer and temperature
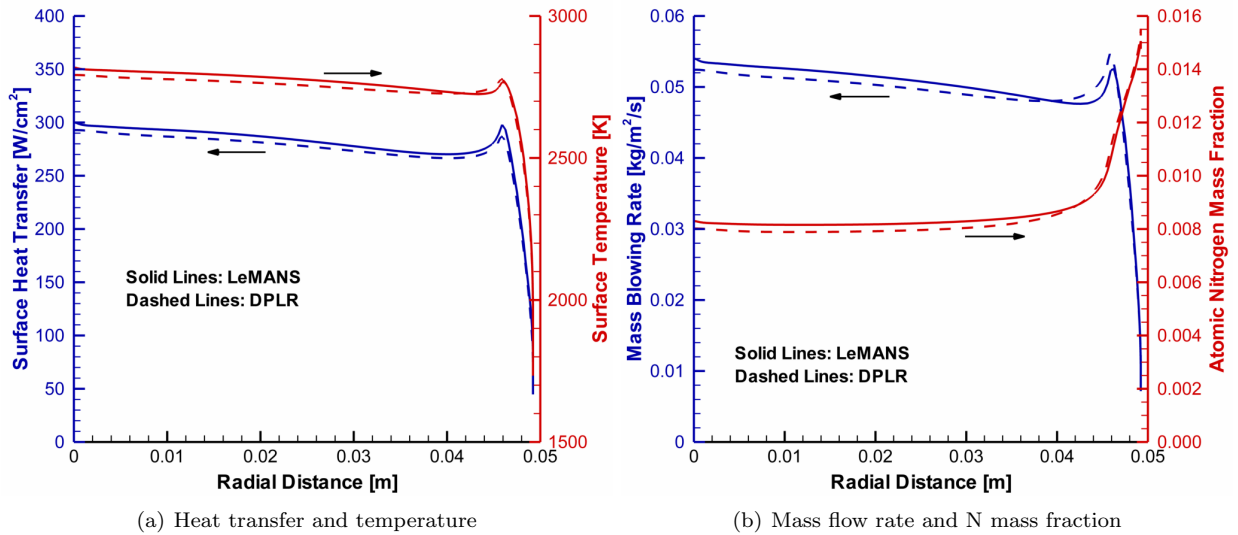
(b) Mass flow rate and N mass fraction

Figure 5: Comparison of heat flux, temperature, mass blowing rate, and nitrogen mass fraction along the iso-Q surface between LeMANS and DPLR for the air/carbon test case.

American Institute of Aeronautics and Astronautics

Table 3: Park's surface chemistry model.

#	Reaction	Type	Parameter	E [kJ/mol]
1	O + (s) + C(b) → CO + (s)	ER	$\gamma_0 = 0.63$	9.644
2	O_2 + 2(s) + 2C(b) → 2CO + 2(s)	ER	$\gamma_0 = 0.50$	0
3	N + (s) + C(b) → CN + (s)	ER	$\gamma_0 = 0.30$	0
4	3(s) + 3C(b) → C_3 + 3(s)	sub	$\gamma_{sub} = 5.19 \times 10^{13}$	775.81

The surface material of the Stardust entry capsule for this study is assumed to be FiberForm, instead of PICA. FiberForm is the substrate from which PICA is processed, and has been shown to have approximately the same properties as the char layer of PICA.[23] This assumption is chosen to neglect the effects of pyrolysis gases since FiberForm does not contain phenolic. The density of the bulk environment is assumed to be equal to 180 kg/m³, which is the density of FiberForm and PICA close to the char exterior surface.[23] The freestream conditions simulated in this study are: $\rho = 1.27 \times 10^{-5}$ kg/m³, $U = 12\,385$ m/s, and $T_{tr} = T_{ve} = 218$ K. These conditions correspond to the 81 km trajectory point, approximately 34 sec after atmospheric entry (see Figure 1(b)). The surface temperature is calculated assuming radiative equilibrium at the wall with an emissivity of 0.9. This is similar to solving Equation 15 and assuming that the enthalpy of the virgin material (i.e. h_a) is equal to the gas phase enthalpy at the wall (i.e. h_w). The mixture transport properties are calculated using Wilke's mixing rule with Blottner's curve fits and Eucken's relation. The Lewis number is assumed to be equal to 1.4.

The chemistry model for the gas environment is adapted from Ref. 24, and consists of the following twenty species:

$$N_2, O_2, NO, N, O, N_2^+, O_2^+, NO^+, N^+, O^+, e$$
$$CO, CO_2, C_3, CN, C, C_2, NCO, CO^+, C^+$$
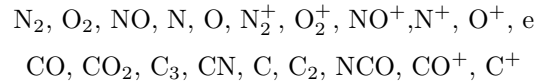
The forward reaction rates are specified in Arrhenius format, $k_f = A T_c^\eta e^{-\frac{T_a}{T_c}}$. They are listed in Table 4, which is also adapted from Ref. 24. Park's two-temperature model[25] is used to set the controlling temperature for each reaction in order to account for the effect of thermal nonequilibrium on the reaction rates.

Table 4: Gas phase chemical reactions (adapted from Ref. 24).

#	Reaction	A [mol,cm,s]	η	T_a [K]
1	N_2 + M ⇌ N + N + M	7.00×10^{21}	-1.6	113200.0
	N, N^+ enhanced by 4.28			
	O, O^+ enhanced by 4.28			
	C, C^+ enhanced by 4.28			
	e enhanced by 428			
2	O_2 + M ⇌ O + O + M	2.00×10^{21}	-1.5	59500.0
	N, N^+ enhanced by 5.00			
	O, O^+ enhanced by 5.00			
	C, C^+ enhanced by 5.00			
3	NO + M ⇌ N + O + M	5.00×10^{15}	0.0	75500.0
	N, N^+ enhanced by 20.0			
	O, O^+ enhanced by 20.0			
	C, C^+ enhanced by 20.0			
4	CO + M ⇌ O + C + M	2.30×10^{19}	-1.0	129000.0
	N, N^+ enhanced by 1.50			
	O, O^+ enhanced by 1.50			
	C, C^+ enhanced by 1.50			
5	NCO + M ⇌ N + CO + M	6.30×10^{16}	-0.5	24000.0
6	CO_2 + M ⇌ O + CO + M	3.50×10^{14}	0.0	52525.0
7	CN + M ⇌ C + N + M	2.53×10^{14}	0.0	71000.0
8	C_2 + M ⇌ 2C + M	4.50×10^{18}	-1.0	70930.0
9	N_2 + O ⇌ N + NO	6.40×10^{17}	-1.0	38370.0

Continued on next page

American Institute of Aeronautics and Astronautics

Table 4 – continued from previous page

#	Reaction	A [mol,cm,s]	η	T_a [K]
10	$NO + O \rightleftharpoons N + O_2$	8.40×10^{12}	0.0	19450.0
11	$C + N_2 \rightleftharpoons CN + N$	5.24×10^{13}	0.0	22600.0
12	$C + NO \rightleftharpoons CN + O$	2.02×10^{14}	-0.3	0.0
13	$C + NO \rightleftharpoons CO + N$	2.29×10^{13}	0.0	0.0
14	$C + O_2 \rightleftharpoons O + CO$	5.80×10^{13}	0.0	576.0
15	$C_2 + C_2 \rightleftharpoons C_3 + C$	3.20×10^{14}	0.0	0.0
16	$C_2 + N_2 \rightleftharpoons CN + CN$	1.50×10^{13}	0.0	21000.0
17	$CN + C \rightleftharpoons C_2 + N$	5.00×10^{13}	0.0	13000.0
18	$CN + CO \rightleftharpoons C + NCO$	1.50×10^{16}	-0.5	65800.0
19	$CN + CO_2 \rightleftharpoons CO + NCO$	4.00×10^{14}	0.0	19200.0
20	$CN + NO \rightleftharpoons N + NCO$	2.00×10^{13}	0.0	21000.0
21	$CN + O \rightleftharpoons CO + N$	2.41×10^{14}	-0.2	0.0
22	$CN + O_2 \rightleftharpoons O + NCO$	1.05×10^{13}	0.0	0.0
23	$CO_2 + O \rightleftharpoons CO + O_2$	2.10×10^{13}	0.0	27800.0
24	$N + CO_2 \rightleftharpoons NO + CO$	3.00×10^{12}	0.0	5690.2
25	$NCO + N \rightleftharpoons N_2 + CO$	2.00×10^{13}	0.0	0.0
26	$NCO + NO \rightleftharpoons N_2 + CO_2$	3.80×10^{18}	-2.0	402.8
27	$NCO + O \rightleftharpoons NO + CO$	2.35×10^{13}	0.0	0.0
28	$NCO + O_2 \rightleftharpoons NO + CO_2$	2.00×10^{12}	0.00	10071.1
29	$N + e \rightleftharpoons N^+ + e + e$	2.5×10^{34}	-3.82	168600.0
30	$O + e \rightleftharpoons O^+ + e + e$	3.9×10^{33}	-3.78	158500.0
31	$C + e \rightleftharpoons C^+ + e + e$	3.7×10^{31}	-3.0	130720.0
32	$O + N \rightleftharpoons NO^+ + e$	5.30×10^{12}	0.0	31900.0
33	$O + O \rightleftharpoons O_2^+ + e$	1.1×10^{13}	0.00	80600.0
34	$N + N \rightleftharpoons N_2^+ + e$	2.0×10^{13}	0.00	67500.0
35	$C + O \rightleftharpoons CO^+ + e$	8.80×10^{8}	1.0	33100.0
36	$C + N \rightleftharpoons CN^+ + e$	1.00×10^{15}	1.50	164000.0
37	$N_2 + O_2^+ \rightleftharpoons N_2^+ + O_2$	9.9×10^{12}	0.00	40700.0
38	$N^+ + N_2 \rightleftharpoons N_2^+ + N$	1.0×10^{12}	0.50	12200.0
39	$CN^+ + N \rightleftharpoons CN + N^+$	9.80×10^{12}	0.0	40700.0
40	$CO + C^+ \rightleftharpoons CO^+ + C$	1.0×10^{13}	0.00	31400.0
41	$NO^+ + C \rightleftharpoons NO + C^+$	1.0×10^{13}	0.00	23200.0
42	$NO^+ + N \rightleftharpoons N_2^+ + O$	7.20×10^{13}	0.0	35500.0
43	$NO^+ + N \rightleftharpoons O^+ + N_2$	3.4×10^{13}	0.00	12800.0
44	$NO^+ + O \rightleftharpoons N^+ + O_2$	1.0×10^{12}	0.50	77200.0
45	$NO^+ + O \rightleftharpoons O_2^+ + N$	7.2×10^{12}	0.29	48600.0
46	$NO^+ + O_2 \rightleftharpoons O_2^+ + NO$	2.4×10^{13}	0.41	32600.0
47	$O^+ + NO \rightleftharpoons N^+ + O_2$	1.4×10^{5}	1.90	15300.0
48	$O^+ + N_2 \rightleftharpoons N_2^+ + O$	9.1×10^{11}	0.36	22800.0
49	$O_2^+ + N \rightleftharpoons N^+ + O_2$	8.70×10^{13}	0.1	28600.0
50	$O_2^+ + O \rightleftharpoons O_2 + O^+$	4.0×10^{12}	-0.09	18000.0
51	$O_2 + C^+ \rightleftharpoons O_2^+ + C$	1.0×10^{13}	0.00	9400.0

The computational mesh used for the numerical simulations of the Stardust forebody geometry is presented in Figure 6(a). The grid contains 200 cells in the axial direction and 240 cells in the radial direction, with clustering near the capsule surface. The grid was generated based on preliminary simulations in order to ensure that solution is mesh independent and that the grid cells are aligned with the bow shock. Figure 6(b) shows qualitative flow field temperature contours for a non-ablative, non-catalytic wall. These contours highlight the alignment of the grid cells with the bow shock, as well as the extreme temperatures reached in the shock layer.

B.   Results

Translational temperature profiles along the stagnation streamline for the two surface chemistry models considered in this study are presented in Figure 7. The figure also presents the distributions for the non-ablative, non-catalytic and fully-catalytic wall boundary conditions. The fully-catalytic wall represents a conservative boundary condition for which all ions recombine to their neutral counterparts (e.g. N^+ to N), and all atoms recombine to molecules (i.e. N to N_2 and O to O_2). Figure 7(a) shows that the peak temperature is approximately 60 000 K for all the cases, with a small difference of 3% between the two finite-rate models. The figure also shows that the surface chemistry model has a slight effect on the bow

American Institute of Aeronautics and Astronautics
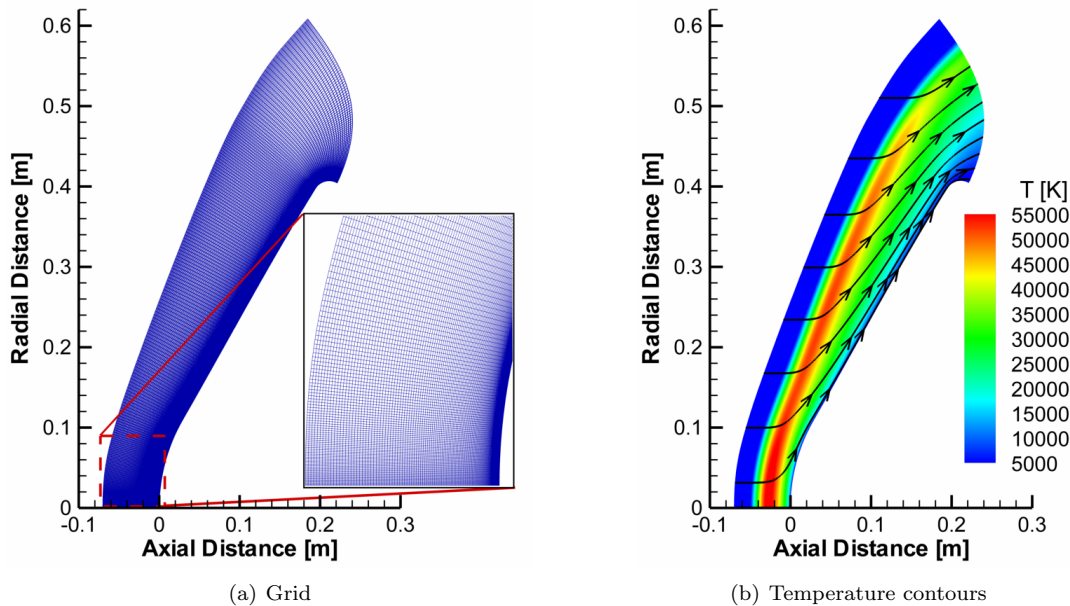
(a) Grid

(b) Temperature contours

Figure 6: Computational grid and temperature contours for the Stardust forebody simulation.

shock standoff distance. Close to the surface in the boundary layer, the surface chemistry model has a more significant effect on the temperature distribution, as can be seen in Figure 7(b). The two finite-rate models decrease both the value and the gradient of the temperature compared to the non-catalytic wall solution. The fully-catalytic wall condition produces the largest temperature value and gradient near the surface. These differences in the temperature profiles also extend to the heat transfer results, as will be shown later.

The mass fractions of neutral air and carbon species in the boundary layer along the stagnation streamline for the two surface chemistry models are presented in Figure 8. Figure 8(a) shows that the mass fraction of O in the boundary layer for Driver's model is slightly larger than for Park's model. The mass fraction of molecular nitrogen is approximately the same for the two models. The nitridation reaction in Park's model consumes more atomic nitrogen than the catalysis reaction in Driver's model, which results in a smaller mass fraction near the surface. Although relatively small for both models, the mass fraction of molecular oxygen for Driver's model is greater than Park's model close to the surface. Figure 8(b) shows that the mass fraction of CN near the surface for Park's model is about six times larger than for Driver's model due to the carbon nitridation reaction. The mass fraction of CO near the surface for Driver's model is approximately 14% larger than for Park's model. Away from the surface, the mass fractions of CN and CO decrease as these species dissociate and form other species, such as C, C_2 and C_3.

Figure 9 presents the heat transfer and temperature along the forebody surface of the Stardust capsule computed using the two finite-rate surface chemistry models considered in this study. The figure also presents the distributions obtained using the non-ablative, non-catalytic and fully-catalytic wall boundary conditions. The heat transfer, shown in Figure 9(a), predicted using Driver's model is about 20% larger than predicted using Park's model over most of the surface. The heat transfer for the non-catalytic wall is closer to the solution for Driver's model near the nose, and in good agreement with Park's model near the shoulder of the capsule. The disagreement between the solutions for the non-catalytic wall (and Park's model) and Driver's model near the shoulder is caused by the recombination of some nitrogen atoms due to the catalysis reaction. The heat transfer for the fully-catalytic wall is greater than the heat flux for the Driver and Park models over the entire surface by approximately 40% and 60%, respectively. These results agree with the trends observed in the boundary layer temperature profiles shown in Figure 7(b); namely that relative to the non-catalytic wall solution, the temperature gradient near the stagnation point is smaller for the two finite-rate surface chemistry models and larger for the fully-catalytic wall. Figure 9(b) presents the surface temperature distributions for the four cases. The figure shows that the surface temperature trends are overall similar to the trends observed in the heat transfer results.
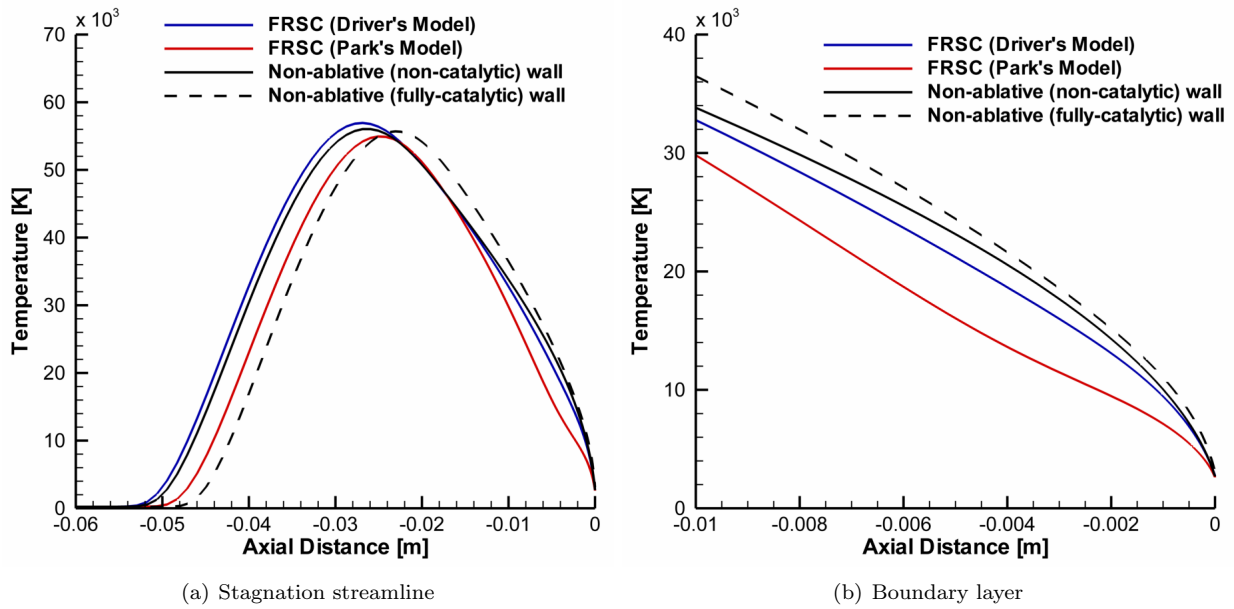
American Institute of Aeronautics and Astronautics

(a) Stagnation streamline

(b) Boundary layer

Figure 7: Translational temperature profiles along the stagnation streamline.

(a) Air species

(b) Carbon species
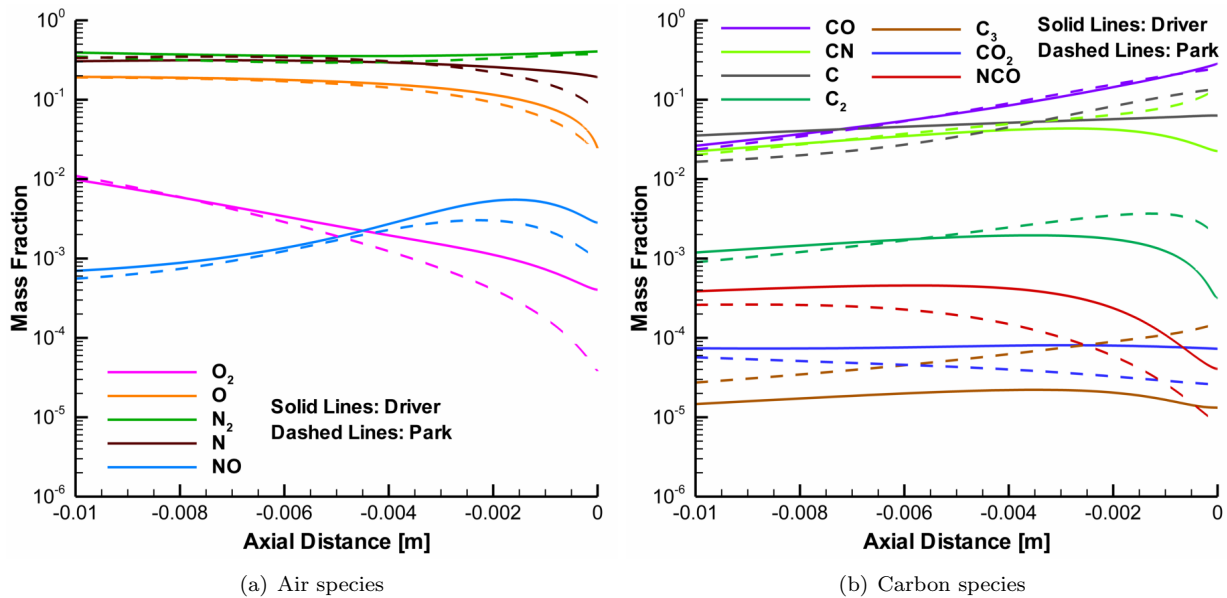
Figure 8: Mass fraction profiles for air and carbon (neutral) species in the boundary layer along the stagnation streamline.
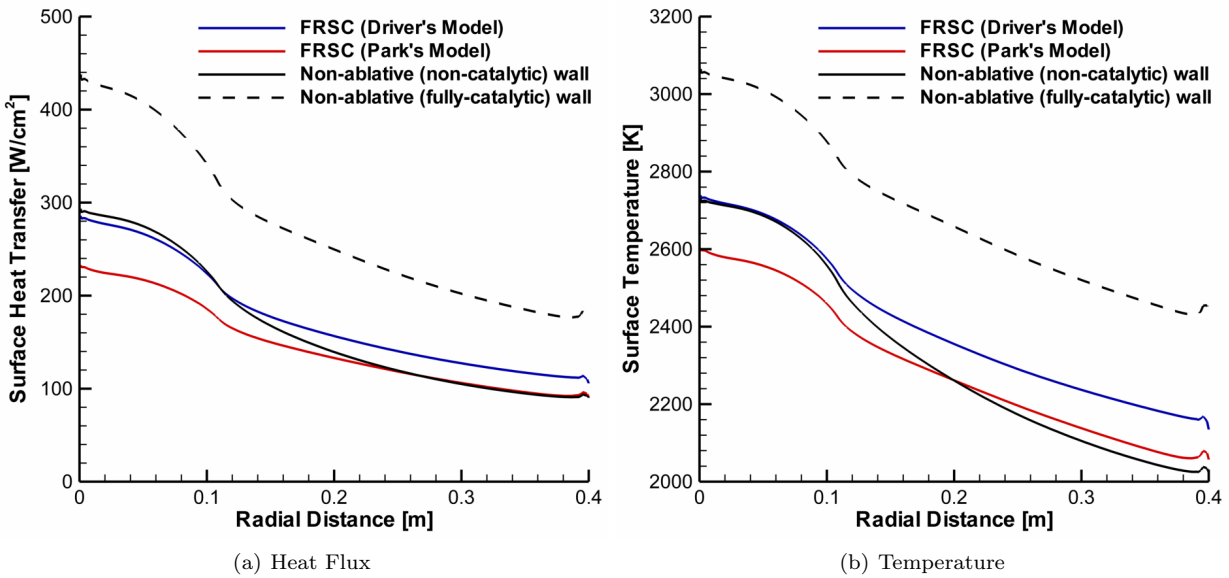
(a) Heat Flux

(b) Temperature

Figure 9: Heat transfer and temperature along the Stardust forebody.

The surface mass blowing rate along the Stardust forebody due to the removal of bulk carbon by the oxidation and nitridation reactions for the Driver and Park models is shown in Figure 10. For Park's model, Figure 10(b) also shows the mass blowing rates for CO and CN. The C_3 mass blowing rate for Park's model is small and is not included in the figure. The blowing rate for both models is largest at the stagnation point and decreases closer to the shoulder of the capsule. The surface blowing decreases the temperature gradient near the surface (as shown in Figure 7(b)), which reduces the heat transfer to the vehicle surface. The total mass blowing rate for Park's model is about 45% larger than the blowing rate for Driver's model. As a result, the heat transfer for Park's model is less than the heat transfer for Driver's model. Figure 10(b) shows that the contribution of the CN blowing rate due to carbon nitridation to the total blowing rate is almost 80% for Park's model. The mechanism for the production of CN included in Park's model increases the mass blowing rate, which decreases the heat transfer to the surface compared to Driver's model.
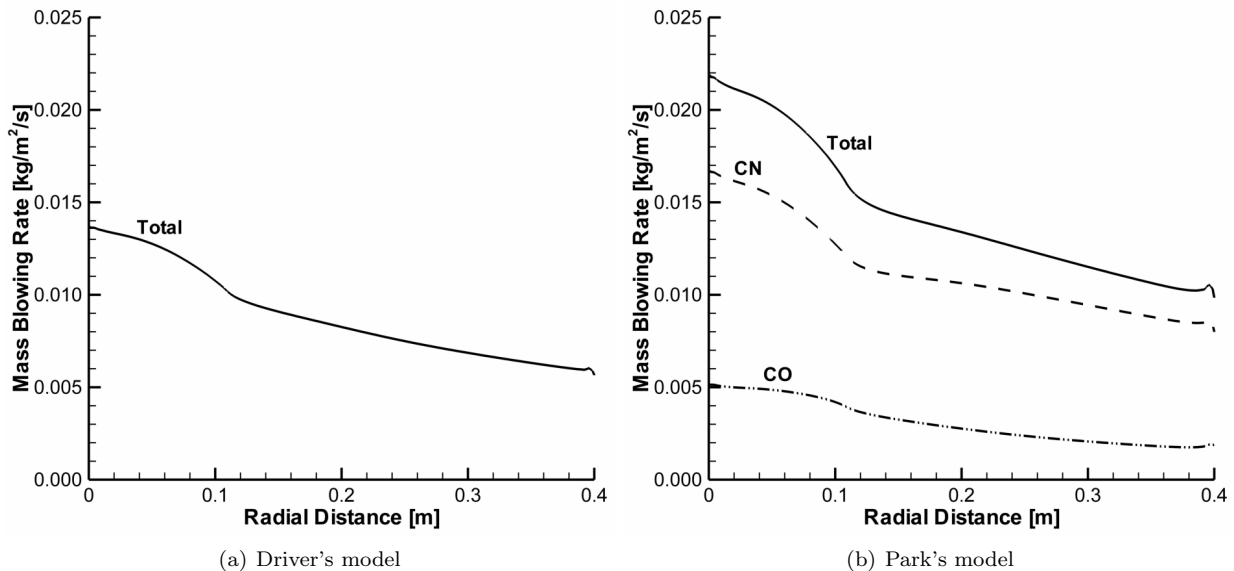

(a) Driver's model

(b) Park's model

Figure 10: Mass blowing rate along the Stardust forebody.

American Institute of Aeronautics and Astronautics

The reaction efficiencies for the two surface chemistry models can be demonstrated by examining the effective loss efficiency of the gas phase reactants along the Stardust forebody, defined in Equation 16. Figure 11 presents the effective loss efficiency of O, O_2, and N, and the molar production rates of CO, CN, and N_2, along the surface for the Driver and Park models. As expected, the effective loss efficiencies for Driver's model are constant and equal to the corresponding reaction efficiencies given in Table 2. The effective loss efficiencies of O_2 and N for Park's model are also constant and equal to the corresponding efficiencies listed in Table 3. The effective loss efficiency of atomic oxygen for Park's model is approximately constant and equal to about 0.4. Figure 11(b) shows that the CO production rate for Driver's model is more than twice as large as the CO production rate for Park's model. The production rate of CN for Park's model is relatively large, and in fact, is about three times greater than the production rate of CO. The CN production rate is also large compared to the production rate of CO for Driver's model by approximately 20%. The significant CN production rate can be attributed to the relatively large efficiency of the carbon nitridation reaction ($\gamma_{ni,N} = 0.3$) and the abundance of atomic nitrogen in the shock and boundary layers, as shown in Figure 8(a). Figure 11(b) also shows that the production rate of N_2 for Driver's model due to the nitrogen catalysis reaction is approximately constant and equal to 0.3 mol/m^2/s. The catalysis of nitrogen increases the heat transfer to the surface, which can also contribute to the difference between the Driver and Park models. The production rate of C_3 from the sublimation reaction for Park's model is very small ($\sim 10^{-4}$ mol/m^2/s) and has been excluded in Figure 11(b).

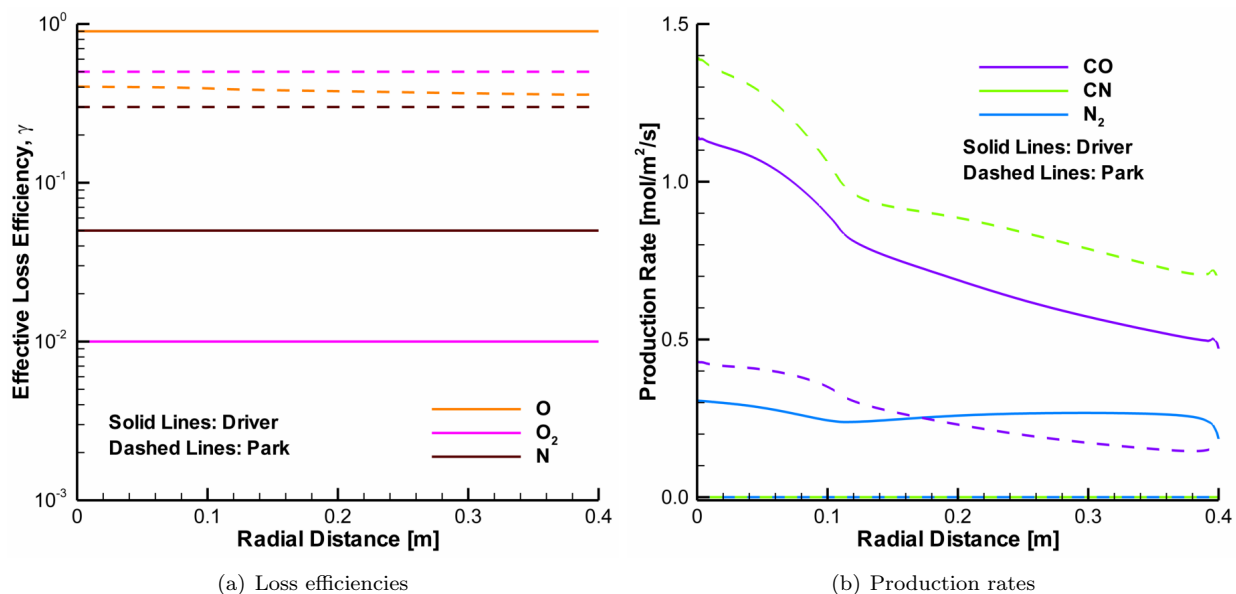(a) Loss efficiencies

(b) Production rates

Figure 11: Effective loss efficiency and species production rates along the Stardust forebody.

In order to quantify the effects of carbon nitridation in Park's model, Figure 12 presents the heat transfer and mass blowing rate for Driver's model and Park's model with and without carbon nitridation (i.e. excluding Reaction # 3 in Table 3). The heat transfer for Park's model without carbon nitridation is in better agreement with Driver's model. Figure 12(a) shows that the difference between the Driver and Park models decreases to approximately 8% near the nose when carbon nitridation is excluded. Near the shoulder, however, the effects of the carbon nitridation reaction are small and the difference between the Driver and Park models is 20%. This difference is possibly caused by the mechanism for nitrogen catalysis included in Driver's model. Figure 12(b) also shows good agreement in the blowing rate predicted by Driver's model and Park's model without nitridation, which can be expected since the models use overall similar reaction efficiencies for carbon oxidation.
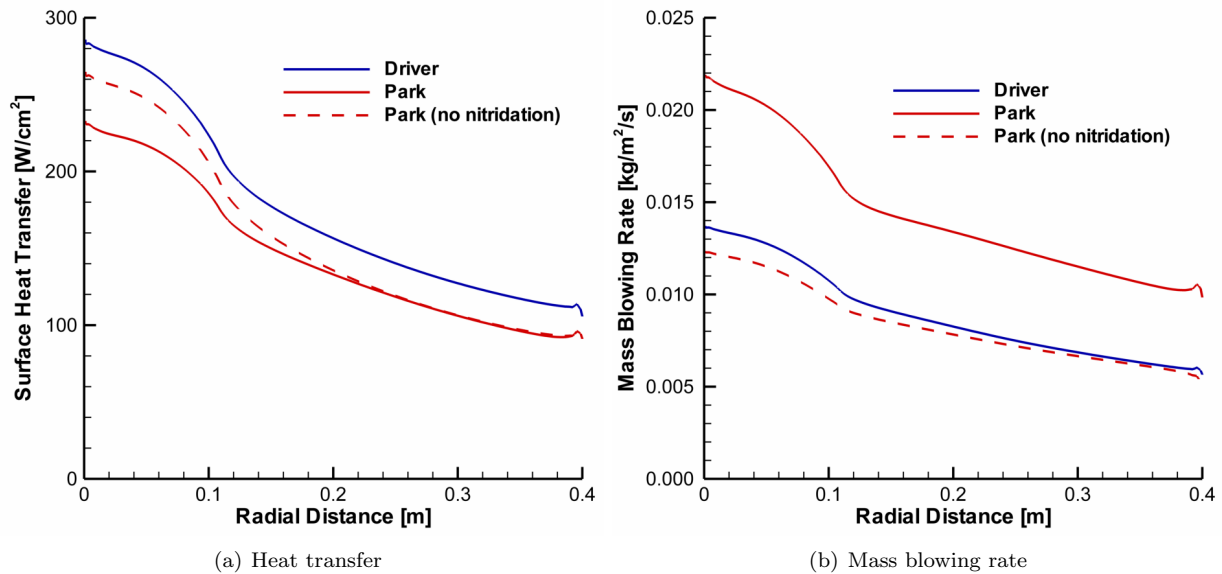
American Institute of Aeronautics and Astronautics

(a) Heat transfer

(b) Mass blowing rate

Figure 12: Effects of carbon nitridation on the heat transfer and mass blowing rate along the Stardust forebody.

V.   Conclusion

A finite-rate surface chemistry module, developed by Marschall and MacLean, has been coupled to the Navier-Stokes code LeMANS. The module simulates the local interactions between the hypersonic gas flow and the surface of a planetary entry vehicle. The module allows for the definition of several different surface reaction mechanisms, such as adsorption, Eley-Rideal recombination, Langmuir-Hinshelwood recombination, and sublimation. The first part of this study presented a brief overview of the formulation used in the FRSC Module and provided details regarding its coupling to LeMANS. Excellent agreement in code-to-code comparisons between LeMANS and DPLR for two different test cases indicated that the coupling of the FRSC Module is accurate.

The second part of this study described a comparison of the flow field and surface properties for the Stardust entry capsule at the 81 km trajectory point obtained using two different surface chemistry models. The first model, developed by Driver et al., includes catalysis of nitrogen and carbon oxidation by atomic and molecular oxygen. The second one is Park's model, which includes carbon oxidation and nitridation, as well as sublimation. The results showed that the production of CN in Park's model causes the mass blowing to be greater by as much as 45% compared to Driver's model. The heat transfer to the surface for Park's model was approximately 20% less than Driver's model. The difference in the heat transfer between the two models could be caused by the carbon nitridation reaction in Park's model, which decreases the heat flux, and the nitrogen catalysis reaction in Driver's model, which increases the heat flux. When the carbon nitridation reaction is excluded from Park's model, the results showed better agreement to Driver's model in the heat transfer near the nose of the capsule and the mass blowing rate along most of the forebody.

For future work, the mixture transport properties will be determined using more accurate models, such as Gupta's mixing rule with collision cross section data for the mixture viscosity and thermal conductivity, and the self-consistent effective binary diffusion method[26, 27] for the mass diffusion fluxes. In the current study, the gas phase surface temperature is assumed to be equal to the temperature at the wall. Future studies can investigate the effects of temperature jumps at the surface on the predicted flow field and surface properties. Finally, the effects of nonequilibrium pyrolysis, spallation and charring, and multi-scale radiation will be evaluated by coupling LeMANS with the FRSC Module to a material response solver and a radiation code.

American Institute of Aeronautics and Astronautics

Acknowledgments

References

[1] Marschall, J. and MacLean, M., "Finite-Rate Surface Chemistry Model, I: Formulation and Reaction System Examples," *AIAA Paper 2011-3783*, June 2011.

[2] MacLean, M., Marschall, J., and Driver, D. M., "Finite-Rate Surface Chemistry Model, II: Coupling to Viscous Navier-Stokes Code," *AIAA Paper 2011-3784*, June 2011.

[3] Scalabrin, L. C., *Numerical Simulation of Weakly Ionized Hypersonic Flow Over Reentry Capsules*, Ph.D. thesis, The University of Michigan, 2007.

[4] Martin, A., Scalabrin, L. C., and Boyd, I. D., "High Performance Modeling of Atmospheric Re-entry Vehicles," *Journal of Physics: Conference Series*, Vol. 341, No. 1, 2012, Article 012002.

[5] Olynick, D., Chen, Y.-K., and Tauber, M. E., "Aerothermodynamics of the Stardust Sample Return Capsule," *Journal of Spacecraft and Rockets*, Vol. 36, No. 3, May-June 1999, pp. 442–462.

[6] Tran, H. K., Johnson, C. E., Rasky, D. J., Hui, F. C. L., Hsu, M.-T., and Chen, Y. K., "Phenolic Impregnated Carbon Ablators (PICA) for Discovery class missions," *AIAA Paper 1996-1911*, June 1996.

[7] Wright, M. J., Candler, G. V., and Bose, D., "Data-Parallel Line Relaxation Method for the Navier-Stokes Equations," *AIAA Journal*, Vol. 36, No. 9, September 1998, pp. 1603–1609.

[8] Driver, D. M., Olsen, M. W., Barnhardt, M. D., and MacLean, M., "Understanding High Recession Rates of Carbon Ablators Seen in Shear Tests in an Arc Jet," *AIAA Paper 2010-1177*, January 2010.

[9] Driver, D. M. and MacLean, M., "Improved Predictions of PICA Recession in Arc Jet Shear Tests," *AIAA Paper 2011-141*, January 2011.

[10] Park, C. and Ahn, H., "Stagnation-Point Heat Transfer Rates for Pioneer-Venus Probes," *Journal of Thermophysics and Heat Transfer*, Vol. 13, No. 1, 1999, pp. 33–41.

[11] Park, C., "Calculation of Stagnation-Point Heating Rates Associated with Stardust Vehicle," *AIAA Paper 2005-0190*, January 2005.

[12] Chen, Y.-K. and Milos, F. S., "Navier-Stokes Solutions with Finite Rate Ablation for Planetary Mission Earth Reentries," *Journal of Spacecraft and Rockets*, Vol. 42, No. 6, 2005, pp. 961–970.

[13] McBride, B. J., Zehe, M. J., and Gordon, S., "NASA Glenn Coefficients for Calculating Thermodynamic Properties of Individual Species," NASA/TP-2002-211556, National Aeronautics and Space Administration, September 2002.

[14] Wilke, C. R., "A Viscosity Equation for Gas Mixtures," *Journal of Chemical Physics*, Vol. 18 No. 4, 1950, pp. 517–519.

[15] Blottner, F. G., Johnson, M., and Ellis, M., "Chemically Reacting Viscous Flow Program for Multi-Component Gas Mixtures," SC-RR-70-754, Sandia Laboratories, Albuquerque, New Mexico, 1971.

[16] Vincenti, W. G. and Kruger, C. H., *Introduction to Physical Gas Dynamics*, Krieger Publishing Company, 2002.

[17] Gupta, R. N., Yos, J. M., Thompson, R. A., and Lee, K.-P., "A Review of Reaction Rates and Thermodynamic and Transport Properties for an 11-Species Air Model for Chemical and Thermal Nonequilibrium Calculations to 30000 K," NASA-RP-1232, National Aeronautics and Space Administration, 1990.

[18] Sutton, K. and Gnoffo, P. A., "Multi-Component Diffusion with Application to Computational Aerothermodynamics," *AIAA Paper 1998-2575*, June 1998.

[19] MacCormack, R. W. and Candler, G. V., "The Solution of the Navier-Stokes Equations using Gauss-Seidel Line Relaxation," *Computers and Fluids*, Vol. 17, 1989, pp. 135–150.

[20] Karypis, G. and Kumar, V., "METIS: A Software Package for Partitioning Unstructured Graphs, Partitioning Meshes, and Computing Fill-Reducing Orderings of Sparse Matrices," *University of Minnesota*, 1998.

[21] Rindal, R. A., Flood, D. T., and Kendall, R. M., "Analytical and Experimental Study of Ablation Material for Rocket-Engine Application," NASA CR-54757, ITEK Corporation, May 1966.

[22] Sorensen, C., Valentini, P., and Schwartzentruber, T. E., "Uncertainty Analysis of Reaction Rates in a Finite Rate Surface Catalysis Model," *AIAA Paper 2011-3643*, June 2011.

[23] Stackpoole, M., Sepka, S., Cozmuta, I., and Kontinos, D., "Post-flight Evaluation of Stardust Sample Return Capsule Forebody Heatshield Material," *AIAA Paper 2008-1202*, January 2008.

[24] Martin, A., Boyd, I. D., Cozmuta, I., and Wright, M. J., "Chemistry Model for Ablating Carbon-Phenolic Material During Atmospheric Re-entry," *AIAA Paper 2010-1175*, January 2010.

[25] Park, C., *Nonequilibrium Hypersonic Aerothermodynamics*, John Wiley and Sons, 1990.

[26] Ramshaw, J. D. and Chang, C. H., "Friction-Weighted Self-Consistent Effective Binary Diffusion Approximation," *Journal of Non-Equilibrium Thermodynamics*, Vol. 21, 1996, pp. 223–232.

[27] Ramshaw, J. D. and Chang, C. H., "Ambipolar Diffusion in Two-Temperature Multicomponent Plasmas," *Plasma Chemistry and Plasma Processing*, Vol. 13, No. 3, 1993, pp. 489–498.

American Institute of Aeronautics and Astronautics